385

Buscheck

UCID-21571

SCP
5-1765

Preliminary Scoping Calculations of Hydrothermal Flow in Variably Saturated, Fractured, Welded Tuff During the Engineered Barrier Design Test at the Yucca Mountain Exploratory Shaft Test Site

Thomas A. Buscheck
John J. Nitao

November, 1988

Lawrence Livermore National Laboratory

Work performed under the auspices of the U.S. Department of Energy by the Lawrence Livermore National Laboratory under Contract W-7405-Eng-48.

Preliminary Scoping Calculations of Hydrothermal Flow in Variably Saturated, Fractured, Welded Tuff During the Engineered Barrier Design Test at the Yucca Mountain Exploratory Shaft Test Site

Thomas A. Buscheck and John J. Nitao

Lawrence Livermore National Laboratory

ABSTRACT

A primary objective of the Engineered Barrier Design Test (EBDT) at the Yucca Mountain Exploratory Shaft Test Site is to examine how the variably saturated, fractured rock mass surrounding the waste package will respond hydrothermally to heating, cooling, and infiltration. The EBDT will include several partial- and/or full-scale electrical heaters to simulate the thermal load generated by the waste packages. An extensive network of geophysical instruments will monitor changes in the temperature, pressure, and saturation distributions in the area around the heaters during the heating and cooling phases of the experiment. The design of the network requires advance knowledge of the spatial and temporal changes in these properties, as well as the ranges in these properties. We model this hydrothermal system as a discrete fracture/matrix system, using the integral finite difference code TOUGH and the best available data on the fracture and matrix properties of Topopah Spring densely welded tuff. These calculations will also be useful for the design of the underground facilities in the vicinity of the EBDT; e.g., in determining the volume of undisturbed rock required for each EBDT heater. After conceptualizing our model to be an infinitely long heater (either horizontal or vertical) which is orthogonally intersected by an infinite set of uniformaly spaced fractures, we justify its applicability to both horizontal and vertical heater emplacement. The calculations show that by the end of the full-power heating stage (t = 6 months), boiling in the rock results in complete desaturation out to a radius of r = 0.8 m from the heater axis, with partial desaturation occuring out to r = 1.8 m. Water vapor which does not leave the system via the borehole (to the drift) moves radially outward to the condensation zone lying 1.8 to 4.0 m from the heater axis. Gas pressures build up considerably within the matrix due to the low matrix permeability, but remain close to ambient within the fracture due to the high fracture permeability. At the end of the cooling stage (t = 24 months), the saturation in the matrix is below ambient for r < 3.0 m. Maximum temperature changes (above ambient) are 252.6 °C at the borehole wall, and 10.2 °C at a radial distance of 10.0 m from the heater axis.

Work performed under the auspices of the U.S. Department of Energy by Lawrence Livermore National Laboratory under Contract W-7405-Eng-48.

Table of Contents

List of Figures

1. Introduction

The Yucca Mountain Project (YMP) of the U.S. Department of Energy (DOE) is investigating the feasibility of constructing and operating a high-level nuclear waste repository in tuffaceous rocks occurring in the unsaturated zone at Yucca Mountain, Nevada. The YMP project has assigned Lawrence Livermore National Laboratory (LLNL) the task of designing and assessing the expected performance of waste packages in the repository environment.

Reliably assessing waste package performance requires, among other things, accurate characterization of the thermal and hydrologic properties of the near-field geologic environment. Various *in situ* tests will be conducted in the Exploratory Shaft within the Topopah Spring member of the Paintbrush Tuff at Yucca Mountain. A primary objective of the Engineered Barrier Design Test (EBDT) is to examine how the variably saturated, fractured rock mass surrounding the waste package will respond to heating, cooling, and infiltration (Yow, 1985). In addition, data from the EBDT will be used in validating near-field flow and transport models. Results obtained from these validated models will then be used to develop the flow and transport modules of the waste package performance assessment model.

The EBDT will simulate the thermal load generated by the waste packages with several partial- and/or full-scale electrical heaters emplaced both horizontally and vertically. An extensive network of geophysical instruments will monitor changes in the temperature, pressure, and saturation distributions in the area around the heaters during heating and cooling stages of the EBDT. The network design requires advance knowledge of the spatial and temporal changes in these properties, as well as the ranges in these properties. The preliminary scoping calculations of hydrothermal flow described in this report will also be useful for designing the underground facilities in the vicinity of the EBDT; e.g., in determining the volume of undisturbed rock required for each EBDT heater.

The Topopah Springs formation consists of densely welded tuff which is believed to be highly fractured. These fractures serve as major conduits for fluid flow and must therefore be accounted for in both near-field and repository-scale models. Because of the low surface recharge rate, the rock at the repository horizon is only partially saturated, and multiphase flow of air, water vapor, and liquid water is therefore possible. Heat generated by the waste package can lead to water vaporization and vapor flow in the matrix and fractures. Condensation of

this vapor outside the boiling zone and capillary-driven flow of liquid water can result in the development of a "heat-pipe" (Preuss, Tsang, and Wang, 1984). To account for these conductive, convective, and latent heat transport mechanisms, we use the integral finite difference code TOUGH.

We have conceptualized the physical medium as a discrete fracture/matrix system (Figure 1). As such, we utilize distinct fracture and matrix properties obtained from Topopah Springs tuff. This approach is well suited to small-scale systems in which the fracture spacing is large in comparison to the scale of the simulation domain. Others (e.g., Nitao, 1988) have accounted for the effects of fracture and matrix flow using the equivalent continuum approach. This approach is well suited for situations in which the fracture spacing is much smaller than the simulation domain. In our system, the fracture spacing is not expected to be small in comparison with the domain over which hydrothermal perturbations occur. Moreover, the pressures, saturations, and temperatures calculated by the equivalent continuum approach are not truly representative of the conditions in either the fractures or matrix. Because our calculations are to be used in assuring that the instruments surrounding the heater are adequately sensitive to the range of pressures, temperatures, and saturations to be encountered, our model must be sufficiently resolved to indicate small-scale variations.

2. Code Description

All numerical calculations were carried out using LLNL's version of the TOUGH ("transport of unsaturated groundwater and heat") code (Nitao, 1988; Buscheck and Nitao, 1987a). TOUGH is a multidimensional numerical simulator capable of modeling the coupled transport of water, vapor, air, and heat in fractured porous media. A member of the Mulkom family of multiphase, multicomponent codes developed at Lawrence Berkeley Laboratory by Preuss (1985), TOUGH has seen previous use in studies of high-level nuclear waste isolation in variably saturated geological media (Preuss, Tsang, and Wang, 1984; Tsang and Preuss, 1986).

The TOUGH code accounts for liquid- and gaseous-phase fluid flow under pressure, viscous, and gravity forces according to Darcy's Law, with interference between phases represented by relative permeability versus saturation curves for the respective phases. The code simultaneously solves three balance (continuum) equations for three components: air mass, water mass, and energy. The combined effects of capillarity and phase adsorption are

accounted for in the moisture retention curves, which plot suction pressure versus saturation. Hysteresis is not accounted for in either the moisture retention or relative permeability curves. Vapor pressure lowering due to capillarity is accounted for using Kelvin's equation (Edlefsen and Anderson, 1943). In addition to binary diffusion in the gas-phase, there is an option to include the effect of Knudsen diffusion, which is also called the Klinkenberg effect (Klinkenberg, 1941). An equation-of-state table-look-up algorithm accurately determines the thermophysical properties of liquid water and vapor based on experimentally derived steam tables (International Formulation Committee, 1967). Air is treated as an ideal gas, and air dissolution in water is represented by Henry's Law. Heat transport mechanisms include conduction (with thermal conductivity dependent on water saturation) and convection (which includes both sensible and latent heat). The code does not account for hydrodynamic dispersion in either the air or water component mass balance equations or in the energy balance equation.

The governing mass- and energy-balance continuum equations are discretized in space using the "integral finite difference" method (Edwards, 1972; Narasimhan and Witherspoon, 1976). Time is discretized in a fully implicit manner. To handle the strongly coupled, highly nonlinear interdependence of mass and heat flow, TOUGH performs a completely simultaneous solution of the discretized governing equations, taking all coupling terms into account. The nonlinearities are handled by Newton/Raphson iteration, and in LLNL's version of TOUGH the solution matrix is inverted using a block-banded Gaussian elimination scheme (Nitao, 1988; Buscheck and Nitao, 1987a). The TOUGH code provides the option of setting the upstream weighting factor, WUP, where $0 \leq \text{WUP} \leq 1$. For this study (as in Buscheck and Nitao, 1987b, 1988) the commonly used, single point, full "upstream weighting" scheme was employed to evaluate the mobilities at the gridblock interfaces. Additional details of the TOUGH code can be found in Preuss (1986), Preuss and others (1985), and Nitao (1988).

3. Discussion of Physical Data and Assumptions

3.1 Matrix Properties

The calculations carried out in this study require a number of assumptions regarding the relevant hydrologic properties and initial and boundary conditions. For sample G4-6 (a sample of Topopah Spring tuff cored at a depth of 1158 feet within the repository interval at Yucca Mountain) Peters and others (1984) obtained matrix porosity, ϕ_m = 11 percent. The initial

saturation of Topopah Spring tuff has not been measured *in situ* at the repository horizon at Yucca Mountain, but has been estimated on the basis of various assumed steady-state infiltration rates. For an assumed infiltration rate of 0.1 *mm/yr*, Wang and Narasimhan (1986) obtain an initial saturation, $S_{wi} \approx 80$ percent. For the same infiltration rate, Nitao (1988) calculated $S_{wi} = 85.4$ percent. For our calculations, we assume $\phi_m = 11$ and $S_{wi} = 85$ percent. Buscheck and Nitao (1988b) considered a range of saturations ($65 < S_{wi} < 85$ percent) in their preliminary scoping calculations of the prototype EBDT in the G-Tunnel complex. Based on their results, we can conclude that varying S_{wi} by 5 percent (i.e., between 80 and 85 percent) does not significantly affect hydrothermal behavior in the vicinity of the heater.

We decided to use the absolute matrix permeability and characteristic curve data obtained by Peters and others (1984) for the Topopah Spring sample G4-6. They obtained their matrix moisture retention curves by applying the curve-fitting method developed by van Genuchten (1980) to their moisture retention data. Their matrix relative permeability curves were not determined directly from experimental data, but rather from their moisture retention curves using the theoretical method of Mualem (1976). While Peters and others (1984) express their characteristic curves as functions of suction pressure, TOUGH requires that they be expressed in terms of saturation (Figures 2 and 3).

3.2 Fracture Properties

For intact fractured samples of Topopah Spring welded tuff (i.e., core samples which have not separated along fractures), Klavetter and Peters (1985) measured fracture apertures ranging from 4.34 to 5.13 μm. Because core samples typically separate in the core barrel along the larger aperture fractures, intact samples tend to reflect only small aperture fractures, thereby biasing out large aperture fractures. Wang and Narasimhan (1985) derived fracture aperture parameters and discrete fracture permeabilities from estimated bulk rock saturated permeabilities reported by Thodarson (1983) and Sinnock, Lin, and Brannen (1984). For Topopah Spring welded tuff they obtained an effective hydraulic aperture of 116 and 150 μm and a discrete fracture permeability of 1.12×10^{-9} and 1.88×10^{-9} m^2 for vertical and horizontal fractures, respectively. They also obtained fracture spacings of 0.22 and 0.48 m for vertical and horizontal fractures, respectively. For our calculations, we assume a fracture aperture of 100 μm and a fracture spacing of 0.3 m.

For this study, we assume that the cubic law is valid for saturated fracture flow. Applying the cubic law to a fracture aperture of 100 μm, we obtain a fracture permeability of 8.3 x 10^{-10} m^2 for a single, saturated fracture. The effects of partial saturation in the fracture are accounted for with the use of a fracture relative permeability curve (Figure 4) used by Buscheck and Nitao (1988) to model a 100 μm fracture. It should be noted that there is no physical data upon which to base the characteristic curves in the fractures. The fracture relative permeability curve was estimated by Wang and Narasimhan (1986) based on a simple conceptual model of fracture flow. For both the fracture and matrix, the sum of the gas- and liquid-phase relative permeabilities always equals one.

We apply the fracture moisture retention curve (Figure 5) used by Buscheck and Nitao (1988) to model a 100 μm fracture. This curve was extrapolated, using the Young-Laplace equation (Adamson, 1982), from a moisture retention curve which Wang and Narasimhan (1986) estimated on the basis of a simple conceptual model of fracture flow. The sharp contrast in the moisture retention curves for the fracture and matrix result in the initial fracture saturation being zero.

3.3 Summary of Model Input Parameters

The model input parameters used in these calculations are summarized below. With the exception of the matrix porosity and fracture spacing, these property values are identical to those used by Buscheck and Nitao (1988).

Rock Properties

- fracture permeability 8.33 x 10^{-10} m^2
- matrix permeability 1.90 x 10^{-18} m^2
- fracture aperture 100.0 μm
- fracture spacing 0.3 m
- matrix porosity 11.0 percent
- thermal conductivity:

  (linear in saturation between wet and dry values)

  wet thermal conductivity: 2.34 $\frac{W}{m°K}$

  dry thermal conductivity: 1.74 $\frac{W}{m°K}$

- density of rock: $2580.0 \frac{kg}{m^3}$
- specific heat of rock: $840.0 \frac{J}{kg°K}$

Initial Conditions

- matrix saturation 85.0 percent
- fracture saturation 0.0 percent
- pressure $1.0 \times 10^5 Pa$
- temperature 23.0 °C

Binary Diffusion

- The binary diffusion coefficient is given in units of $\frac{m^2}{s}$ by the correlation:

$$D = \frac{4.40 \times 10^{-6} (T+273.15)^{2.334}}{p}$$

where T is in degrees Kelvin and p is in Pascals.

3.4 Conceptual Model, Boundary Conditions, and Numerical Grid

Although design specifications for the EBDT heaters are not yet final, preliminary plans (Yow, 1985) are to drill both horizontal and vertical heater boreholes approximately 12.2 m into the rock mass. Only the bottommost 6.1 m of the heater borehole are being considered for heating in order to minimize the interference with the temperature and humidity conditions in the drifts. Preliminary plans call for a partial-scale 0.3-m-diameter heater borehole. Although not planned at the present, it is likely that the EBDT will provide for at least one full-scale heater emplaced in a 0.69-m-diameter borehole that will be used during performance confirmation. One of the purposes of this larger borehole test is to investigate the impact of borehole size and test duration on the conclusions drawn from the EBDT. For this report we considered a partial-scale 0.25-m-diameter heater emplaced in a 0.3-m-diameter borehole.

As will be shown in the following section, significant changes in the gas pressure, temperature, and saturation distributions occur within 3 to 4 m (radially) of the EBDT heater. If the heater is 6.1 m long, the shape of the hydrothermally perturbed zone is reasonably slender. Therefore, within this zone and along the middle of the heater, conditions during (at least) the heating stage resemble those which would result from an infinitely long cylindrical heat source.

Consequently, we assumed that the heater is infinitely long, thereby simplifying the domain of our numerical model. Because they pertain to estimating the volume of undisturbed rock required for each EBDT heater, these calculations can be considered to be conservative.

We have conceptualized our model to consist of an infinitely long heater (Figure 1) which is orthogonally intersected by uniformly spaced fractures. We decided, for the purpose of scoping calculations, to neglect the effect of gravity, thereby allowing us to take advantage of axial symmetry about the heater axis. Therefore, our model employs a two-dimensional $r-z$ coordinate system with the z-axis coinciding with the heater axis and the r-axis coinciding with the midplane of the fracture (Figure 1). Owing to very strong suction forces and low permeabilities in the matrix, the no-gravity assumption appears to be applicable to matrix flow. The applicability of this assumption to fracture flow in the vicinity of the heater will be addressed in a forthcoming report. Based on the no-gravity assumption, our model applies either to the case of a vertically emplaced heater intersected by horizontal fractures or to the case of an horizontally emplaced heater intersected by vertical fractures. Since Scott and Castellanos (1984) observed that the majority of fractures at Yucca Mountain are vertical, our model more realistically pertains to a horizontal heater intersected by vertical fractures.

Although we have not addressed the case of a vertical heater within a network of vertical fractures, based on the following reasoning, we expect that these calculations are adequately representative of the vertical emplacement case. Given (1) reasonable randomness in the distribution of fracture azimuth and (2) a spatial distribution of fracture spacing which does not deviate substantially from 3.3 fractures per meter, a set of vertical fractures should provide an adequate radial component of fracture permeability in all directions surrounding the heater. Instead of flowing exclusively within individual fractures (as would occur in the case of a heater orthogonally intersected by fractures), radial fracture flow occurs over a network of intersecting vertical fractures. While investigating the parameter sensitivity of hydrothermal flow during the prototype EBDT, Buscheck and Nitao (1988b) found that fracture spacing significantly influences boiling within matrix blocks. Therefore, our calculations, whether applied to horizontal or vertical emplacement, are subject to the quality of the available data on fracture spacing (as well as orientation). Given what is currently known about the hydrological conditions at the repository horizon, for scoping purposes, we expect that these calculations are adequately representative of both horizontal and vertical heater emplacement.

The assumption that the parallel fractures in an infinite array are uniformly spaced allows us to employ periodic boundaries in our model. Our model has two planes of symmetry: (1) the plane of symmetry down the center of the fracture and (2) the plane of symmetry down the center of the matrix block separating neighboring fractures. In the numerical mesh, both planes are treated as impermeable, insulated boundaries. The outer radial boundary (located at $r = 20\ m$) is a constant property boundary represented by a large computational boundary block. The heater is a 0.25-m-diameter heat generation cell with a heat generation history (Figure 6) consisting of three stages: (1) the full-power heating stage ($0 < t < 6$ months) during which the heater is at full power (1000 W/m), (2) the "rampdown" stage ($6 < t < 12$ months) during which the heater power is linearly varied from full power to zero, and (3) the cooling stage ($12 < t < 24$ months) during which no heating occurs. Preliminary waste package concepts indicate that the waste package borehole will not be sealed from the drift. Therefore, we assume that the airgap between the heater and borehole wall communicates freely with the drift, which we represent with a large computational boundary block maintained at atmospheric pressure.

Table 1 lists the 21x13 r–z numerical grid spacing used in our model. In the radial direction, the first row of gridblocks ($\Delta r = 0.125\ m$) represents the heater. In the second row of gridblocks (in the radial direction, $\Delta r = 0.025\ m$), which represents the airgap, heat transfer between the heater and borehole wall includes conduction, convection, and radiation. In the radial direction, gridblock rows 3 through 20 represent the fractured rock mass, with row 21 representing the outer radial boundary (with the boundary gridblock centered at $r = 20\ m$). In the axial direction, the first column of gridblocks ($\Delta z = 0.00005\ m$) represents the fracture, with the second through the thirteenth columns representing the matrix.

4. Model Results

Figure 7 plots the temperature history for six different radial locations (including the borehole wall) which lie along the matrix block midplane. At the end of each of the three stages ($t = 6$, 12, and 24 months), temperature is plotted versus radial distance along the matrix block midplane (Figure 8). Figure 9 is a contour plot of temperature within the fracture and matrix at the end of the full-power heating stage ($t = 6$ months). In Figure 9 (as in all contour plots in this report), the fracture midplane lies along the lefthand margin ($z = 0.0\ m$), the matrix block midplane lies along the righthand side ($z = 0.15\ m$), and the axis of the heater

is located along the bottom of the figure (r = 0.0 m). Because temperatures are essentially invariant with respect to axial position in Figure 9 (i.e., distance from the fracture) we can assume that Figures 7 and 8 apply to all axial positions, including the fracture midplane. Before discussing the physical interpretation of the thermal response of the rock to heating, we need to make several observations concerning the saturation and pressure changes.

Figure 10 plots the saturation contours at the end of the full-power heating stage (t = 6 months). Figure 11 plots the radial saturation profile, parallel to and 1 cm from the fracture midplane at the end of each of the three stages (t = 6, 12, and 24 months). Figure 12 plots the radial saturation profile along the midplane of the matrix block. Based on the saturation distribution, we see at t = 6 months that the boiling zone lies within $r < 1.8$ m and that the rock is completely desaturated for $r < 0.8$ m. At the end of the cooling period (t = 24 months) we see that for $r < 3.0$ m, $S_w \leq S_{wi}$. The contour plot of gas-phase pressure (Figure 13) indicates that water vapor in the matrix is driven in three directions: (1) radially inward towards the heater borehole, (2) axially towards the fracture, and (3) radially outward in the matrix. The gas-phase pressure profile along the fracture midplane (Figure 14) indicates that water vapor which has entered the fracture (after leaving the matrix) moves either radially inwards towards the heater borehole or radially outward away from the boiling zone. The water vapor, which has not left the system via the borehole (to the drift), moves radially outward (within the matrix as well as along the fracture) until it is cooled and condenses, forming the condensation zone. At t = 6 months this condensation zone is manifested by a hump in the saturation profile (Figures 11 and 12) occurring in the range $1.8 < r < 4.0$ m.

In Figure 8 we see the impact of saturation conditions on temperature. Because all of the water has been vaporized for $r < 0.8$ m, temperatures are no longer constrained to lie on the two-phase saturation pressure versus temperature curve (Reynolds and Perkins, 1977). Consequently, for $r < 0.8$ m, the temperature profile is very steep, varying between 150 and 275 °C. For $1.6 < r < 1.9$ m, we see two related effects: (1) a flattening in the temperature profile, with $T \approx 100$ °C (Figure 8), and (2) a very steep saturation profile, with $60 < S_w < 95$ percent (Figure 11), indicating the existence of the heat-pipe effect. While the heat-pipe effect may occur within a partially saturated, homogeneous porous medium, its occurence is facillitated (and often more efficient) in situations where two parallel media exist: (1) a coarse-grained porous medium or conduit (e.g., an open fracture) which serves as a conduit for vapor flow

and (2) a fine-grained porous medium which serves as conduit for capillary-driven flow. A heat source located at one end of this system causes water in the fine-grained medium to boil, thereby developing a saturation profile, with saturation increasing with distance from the heat source. Water vapor (leaving the fine-grained medium) enters the coarse-grained medium and is driven away from the heat source out to where it cools, condenses, and is imbibed by the fine-grained medium. Capillarity in the fine-grained medium then drives the water back towards the heat source where it re-boils and is driven away from the heat source, thereby repeating the cycle. Because this counterflow system of vapor and liquid flow provides an extremely efficient means of transporting heat away from the heat source, a very slight (almost flat) temperature gradient can exist in spite of a very large heat flux. We observe in Figures 11 and 12 that the condensation zone occurs just beyond the heat-pipe zone ($r > 1.9\ m$), wherein temperatures gradually decline with distance from the heater (Figure 8).

It is apparent in Figure 10 that the fracture significantly influences the shape of the boiling zone (manifested by fingering of the saturation contours), with boiling occurring more readily at locations closer to the fracture. Figures 15 and 16 are saturation contour plots at the end of the rampdown and cooling stages (t = 12 and 24 months), respectively. By the end of the rampdown stage, it is apparent that the finger in the saturation contours in the vicinity of the fracture has relaxed due to capillary-driven liquid flow. Vapor flow and condensation along the fracture also contributes to the relaxation of the finger in the saturation contours during rampdown and cooling. By the end of the cooling stage, relaxation of the finger in the saturation contours is effectively complete, resulting in the radial saturation profile being invariant with axial distance from the fracture.

In the contour plot of the gas-phase pressure at t = 6 months (Figure 13) we see that, due to the very low matrix permeability, very large gas-phase pressure gradients ($\approx 10\ atm/m$) are required to drive vapor towards the heater borehole and fracture. In Figure 14 we see the influence of the boiling zone moving radially outward (with time) on the radial gas-phase pressure profile along the fracture midplane. We also see that, due to the very large fracture permeability, very small gas-phase pressure gradients are required to drive vapor flow radially inward towards the heater borehole (and out to the drift) and radially outward into the condensation zone.

During the full-power heating stage, boiling and (the resultant) vapor flow displaces essentially all of the air out of the gas-phase within the boiling zone ($r < 1.8\ m$). Consequently, at the end of the full-power heating stage, the gas within the boiling zone is 100 percent water vapor. During the rampdown stage, declining temperatures cause this water vapor within the matrix to condense, thereby causing pressures to drop below atmospheric. By the end of the rampdown stage, this effect manifests itself as a very pronounced low pressure region within the boiling zone in the matrix (Figure 17). This low in the pressure distribution pulls relatively humid air in from the drift, as well as from the condensation zone. The effect of vapor transport and condensation during the cooling stage is manifested by an increase in saturation immediately adjacent to the heater borehole at $t = 24$ months (Figures 11 and 12).

In the plot of temperature versus time (Figure 7) we see that temperatures at the borehole wall increase very rapidly, reflecting the fact that water at this location is vaporized at early time. At $r = 0.75\ m$, temperatures are constrained to lie on the two-phase saturation pressure versus temperature curve until the very end of the full-power heating stage. At $r = 1.05\ m$, temperatures reflect the two-phase conditions which persist throughout heating and cooling. The temperatures at $r = 1.95\ m$ reflect it always being just outside of the boiling zone. Being outside of the zone of significant hydrological perturbations, radial locations $r = 4.1$ and $8.3\ m$ feel the attenuated effects of the heating and cooling cycles. At the borehole wall, the onset of the rampdown stage is immediately felt. For locations in the fractured rock mass, the time at which the peak temperature is attained increases with r.

Table 2 summarizes the maximum property changes in the fractured rock mass for all time. The maximum temperature change occurs at the borehole wall at $t = 6$ months. Because temperatures are essentially invariant with respect to axial location, the maximum temperature change is the same in the fracture and matrix. The maximum pressure change in the matrix occurs at the borehole wall at $t = 30$ days. The location of the maximum pressure change in the fracture moves out radially with time over the period $120.0 < t < 182.5$ days. The maximum change in matrix saturation occurs over the region which has been completely desaturated at $t = 6$ months ($r < 0.8\ m$ in Figure 9). The maximum change in fracture saturation occurs at $r = 2.25\ m$ (within the condensation zone) at $t = 6$ months.

A critical issue to be addressed in the design of the EBDT concerns the volume of undisturbed rock which will be required by each of the EBDT heaters. Interference with the humidity and temperature conditions in the neighboring drifts (as well as interference between neighboring heaters) imposes an additional degree of complexity and uncertainty to the process of validating our models against EBDT data. For example, the appropriate treatment of vapor transport at the rock/drift interface may be difficult to establish. For the time-scale of our scoping calculations, we have (effectively) assumed that the heater lies within a fractured rock mass of infinite radial extent. While interference with the drift may preclude our taking advantage of symmetry in the conceptual and numerical models, it may be relevant to the real case of hydrothermal flow around waste packages. Ideally, full-scale geometries and spacings can be considered without incurring some of the above-mentioned difficulties.

Tables 3 and 4 summarize changes in temperatures and saturations at r = 6.0 and 10.0 m at t = 6 and 24 months. The significance of these two locations stems from the early conceptual design of the EBDT (Yow, 1985). Note that pressure changes at these radial locations and times are negligible. Because the end effects of heating from a finite-length heater are not considered in our model, our estimates become increasingly conservative with time. For locations (axially) beyond the ends of the heater, our estimates are very conservative, particularly during the cooling stage. We see that for both r = 6.0 and 10.0 m, changes in saturation are relatively minor (and are probably comparable to the measurement error). For r = 6.0 m, the temperature change never exceeds 6.7 percent of the maximum temperature change, ΔT_{max}, over the entire fractured rock mass. However, because this change occurs only 6 months into the test, locating a boundary only 6.0 m from the heater should probably be avoided. Because temperature changes at r = 10.0 m never exceed 3.6 percent of ΔT_{max} at t = 24 months (and 1.6 percent of ΔT_{max} at t = 6 months), locating a boundary 10.0 m from the heater should not significantly affect the performance of the hydrothermal field during the EBDT.

5. Summary and Conclusions

The Engineered Barrier Design Test (EBDT) will provide the principal means of investigating the hydrothermal response of the variably saturated, fractured rock mass surrounding the waste packages to heating, cooling, and infiltration events. Moreover, data from the EBDT will be used in validating near-field flow and transport models. These validated models will, in turn, provide data which is required in the development of the flow and transport modules of

the waste package performance assessment model. The success of the EBDT will, in part, depend upon our ability to accurately measure the entire range of temperature, pressure, and saturation conditions in the near-field environment and to avoid undesirable interference effects from the neighboring drifts. Therefore, the design of the EBDT requires advance knowledge of the spatial and temporal changes in these properties, as well as the ranges in these properties. For this purpose, we modeled the heater/fractured rock system with the use of the TOUGH code and the best available data on the fracture and matrix properties of Topopah Spring densely welded tuff cored from the repository horizon. Changes in the temperature, pressure, and saturation distributions are provided for the duration of the heating and cooling stages. Maximum changes in property values, as well as changes at selected locations, are also presented in order to determine the volume of undisturbed rock which will be required by each EBDT heater. The parameter sensitivity of hydrothermal flow around the EBDT heater will be addressed in a forthcoming report.

Acknowledgements

The authors gratefully acknowledge helpful discussions with D. Wilder, A. Ramirez, and W. Daily at Lawrence Livermore National Laboratory. We also appreciate the thoughtful review comments of A. Tompson and R. Knapp at LLNL. We also thank Barbara Strack for her very helpful editorial assistance. This work was support by the Engineered Barrier Design Test task of the Yucca Mountain Project at Lawrence Livermore National Laboratory.

References

Adamson, A. W., "Physical Chemistry of Surfaces", John Wiley and Sons, New York, N. Y., 664 p., 1982.

Aziz, K, and A. Settari, "Petroleum Reservoir Simulation", Applied Science Publishers, Barking, Essex, England, 476 p., 1979.

Buckley, S. E., and M. C. Leverett, "Mechanism of Fluid Displacement in Sands", Transactions of AIME, Vol. 146, pp. 107-116, 1942.

Buscheck, T. A. and J. J. Nitao, "Fluid Flow Modeling", in Institutional Research and Development, FY86 Annual Report, UCRL-53689-86, Lawrence Livermore National Laboratory, Livermore, CA, pp. 48-49, 1987a.

Buscheck, T. A. and J. J. Nitao, "Estimates of the Hydrologic Impact of Drilling Water on Core Samples Taken from Partially Saturated Densely Welded Tuff", UCID-21294, Lawrence Livermore National Laboratory, Livermore, CA, 1987b.

Buscheck, T. A. and J. J. Nitao, "Estimates of the Width of the Wetting Zone Along a Fracture Subjected to an Episodic Infiltration Front in Variably Saturated, Densely Welded Tuff", UCID- , Lawrence Livermore National Laboratory, Livermore, CA, 1988.

Buscheck, T. A. and J. J. Nitao, "Preliminary Scoping Calculations of Hydrothermal Flow in Variably Saturated, Fractured, Welded Tuff During the Prototype Engineered Barrier Design Test", UCID-, Lawrence Livermore National Laboratory, Livermore, CA, 1988b.

Daily, W., and A. L. Ramirez, "Preliminary Evaluation of an Electromagnetic Experiment to Map In Situ Water in Heated Welded Tuff", UCRL-96816, Lawrence Livermore National Laboratory, Livermore, CA, 1987.

Dake, L. P., "Fundamentals of Reservoir Engineering", Developments in Petroleum Science, 8, Elsevier Scientific Publishing Company, New York , N. Y., 443 p., 1978.

Edlefsen, N. E., and A. B. C. Anderson, "Thermodynamics of Soil Moisture", Hilgardia, Vol. 15, No. 2, pp. 31-298, 1943.

Edwards, A. L., "TRUMP: A Computer Program for Transient and Steady-State Temperature Distributions in Multi-Dimensional System", National Technical Information Service, UCRL-14754, Rev. II, Springfield, Virginia, 22151, 265 p., 1972.

International Formulation Committee, "A Formulation of the Thermodynamic Properties of Ordinary Water Substance", IFC Secretariat, Dusseldorf, Germany, 1967.

Klavetter, E. A., and R. R. Peters, "Estimation of Hydrologic Properties of an Unsaturated, Fractured Rock Mass", SAND84-2642, Sandia National Laboratories, Albuquerque, N. M., 32 p., 1984.

Klinkenberg, L. J., "The Permeability of Porous Media to Liquids and Gasses", in: API Drilling and Production Practice, pp. 200-213, 1941.

Lawrence Livermore National Laboratory, "Test Plan: Prototype Engineered Barrier Design Testing - Horizontal Emplacement" in the Nevada Waste Management Program Quality Assurance Program Plan, Lawrence Livermore National Laboratory, Livermore, CA, Rev. 0, 033-NNWSI-p11.0, 1987.

Mualem, Y., "A New Model for Predicting the Hydraulic Conductivity of Unsaturated Porous Materials", Water Resources Research., Vol. 12, no. 3, pp. 513-522, 1976.

Narasimhan, T. N., and P. A. Witherspoon, "An Integrated Finite Difference Method of Analyzing Fluid Flow in Porous Media", Water Resources Research, Vol. 12, No. 1, pp. 57-66, 1976.

Nitao, J. J., "Numerical Modeling of the Environment of a Nuclear Waste Package Using the Equivalent Continuum Approximation: Horizontal Emplacement", UCID-21444, Lawrence Livermore National Laboratory, Livermore, CA, 1988 (in preparation).

Peters, R. R., E. A. Klavetter, I. J. Hall, S. C. Blair, P. R. Hellers, and G. W. Gee, "Fracture and Matrix Hydrologic Characteristics of Tuffaceous Materials from Yucca Mountain, Nye County, Nevada", SAND84-1471, Sandia National Laboratories, Albuquerque, N. M., December 1984.

Preuss, K. "Tough User's Guide", LBL-20700, Lawrence Berkeley Laboratory, Berkeley, CA, November 1985.

Preuss, K., Y. W. Tsang, and S. Y. Wang, "Numerical Studies of Fluid and Heat Flow Near High-Level Nuclear Waste Packages Emplaced in Partially Saturated Fractured Tuff", LBL-18552, Lawrence Berkeley Laboratory, University of California, Berkeley, CA, 1984.

Ramirez, A. L., and W. D. Daily, "Preliminary Evaluation of Alterant Geophysical Tomography in Welded Tuff", UCRL-92229, Lawrence Livermore National Laboratory, Livermore, CA, 9 p., 1985.

Ramirez, A. L., and W. D. Daily, "Evaluation of Alterant Geophysical Tomography in Welded Tuff", Journal of Geophysical Research, Vol. 92, No. B8, pp. 7843-7853, July 10, 1987.

Reynolds, W. C. and H. C. Perkins, "Engineering Thermodynamics", McGraw-Hill, New York, 690 p., 1977.

Scott, R. B. and M. Castellanos, "Stratigraphic and Structural Relations of Volcanic Rocks in Drill Holes USW GU-3 and USW G-3, Yucca Mountain, Nye County, Nevada", USGS-OFR-84-491, U. S. Geological Survey, Denver, CO, 1984.

Sinnock, S., Y. T. Lin, and J. P. Brannen, "Preliminary Bounds on the Expected Postclosure Performance of the Yucca Mountain Repository Site, Southern Nevada", SAND84-1492, Sandia National Laboratories, Albuquerque, N. M., 1984.

Tsang, Y. W., and K. Preuss, "A Study of Thermally Induced Convection Near a High-Level Nuclear Waste Repository in Partially Saturated Fractured Tuff", SAND86-7010J, Sandia National Laboratories, Albuquerque, N. M., 1986 (also LBL-21311).

Thordarson, W., "Geohydrologic Data and Test Results from Well J-13, Nevada Test Site, Nye County, Nevada", Water Resources Investigations Report 83-4171, U. S. Geological Survey, Denver, CO, 1983.

Wang, S. Y., and T. N. Narasimhan, "Hydrologic Mechanisms Governing Fluid Flow in Partially Saturated, Fractured, Porous Tuff at Yucca Mountain", SAND84-7202, Sandia National Laboratories, Albuquerque, N. M., 45 p., April 1985.

Wang, S. Y., and T. N. Narasimhan, "Hydrologic Mechanisms Governing Partially Saturated Fluid Flow in Fractured Welded Units and Porous Non-Welded Units at Yucca Mountain", SAND85-7114, Sandia National Laboratories, Albuquerque, N. M., 69 p., October 1986.

van Genuchten, M. Th., "A Closed-Form Equation for Predicting the Hydraulic Conductivity of the Unsaturated Soils", Soil Sci. Soc. Am. J., Vol. 44, pp. 892-898, 1980.

Yow, J., Jr., "Concept for Waste Package Environment Tests in the Yucca Mountain Exploratory Shaft", UCID-20450, Lawrence Livermore National Laboratory, Livermore, CA, 1985.

Table 1

Numerical Grid Spacing
for the Two-Dimensional Fracture/Matrix R-Z Model
(100 μm fracture)

Radial Direction, Δr (m)					
0.125	0.025	0.15	12 x 0.3	0.4	0.8
1.6	3.2	6.4	$1.0x10^{30}$		
Axial Direction, Δz (m)					
0.00005	0.0001	0.0002	0.0004	0.0008	0.0016
0.0032	0.0064	0.0128	0.0256	0.0486	0.05
0.0002					

Table 2

Maximum Property Changes
for all Locations in the Rock
for all Time

Maximum Temperature Change, ΔT_{max} $°C$
252.6 (matrix)
252.6 (fracture)
Maximum Pressure Change, ΔP_{max} Pa
$11.0x10^{5}$ (matrix)
80.0 (fracture)
Maximum Saturation Change, $(\Delta S_w)_{max}$ percent
85.0 (matrix)
10.2 (fracture)

Table 3

Property Changes at the
End of the Full-Power Heating
Phase (t = 6 months)

	Temperature Change, ΔT °C
r = 6.0 m	16.8
r = 10.0 m	4.1
	Saturation Change, ΔS_w percent
r = 6.0 m	0.5
r = 10.0 m	0.1

Table 4

Property Changes at the
End of the Cooling Phase
(t = 24 months)

	Temperature Change, ΔT °C
r = 6.0 m	13.6
r = 10.0 m	9.2
	Saturation Change, ΔS_w percent
r = 6.0 m	1.0
r = 10.0 m	0.3

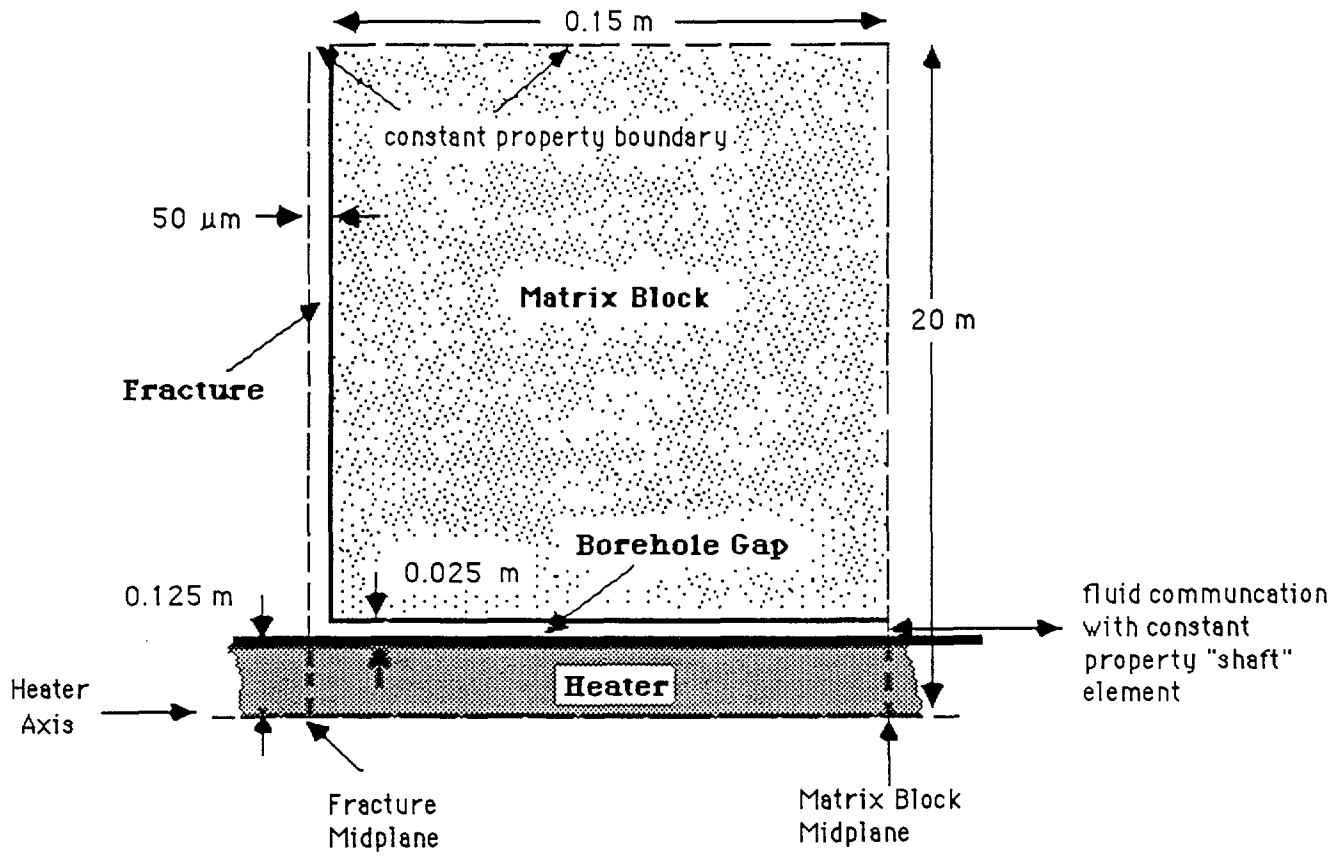

Figure 1. Schematic of the conceptual model used in the simulation. Note that the figure is not to scale.

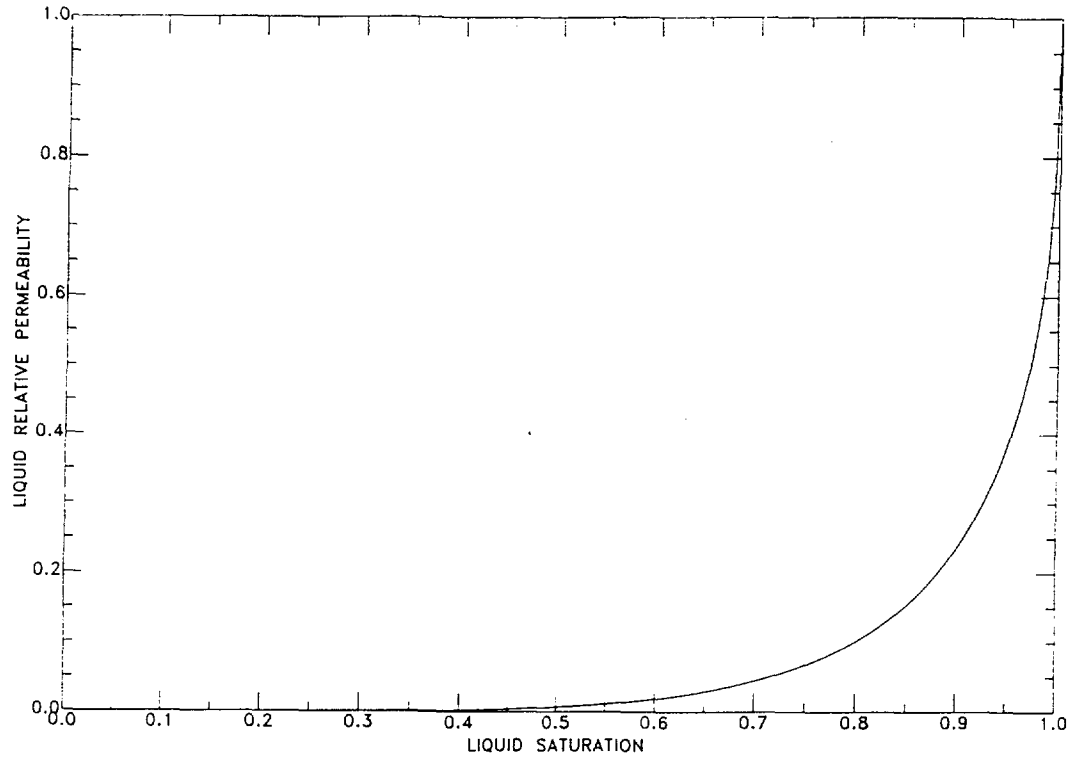

Figure 2. Liquid relative permeability versus liquid saturation for sample G4-6 cored at a depth of 1158 feet within the repository horizon at Yucca Mountain.

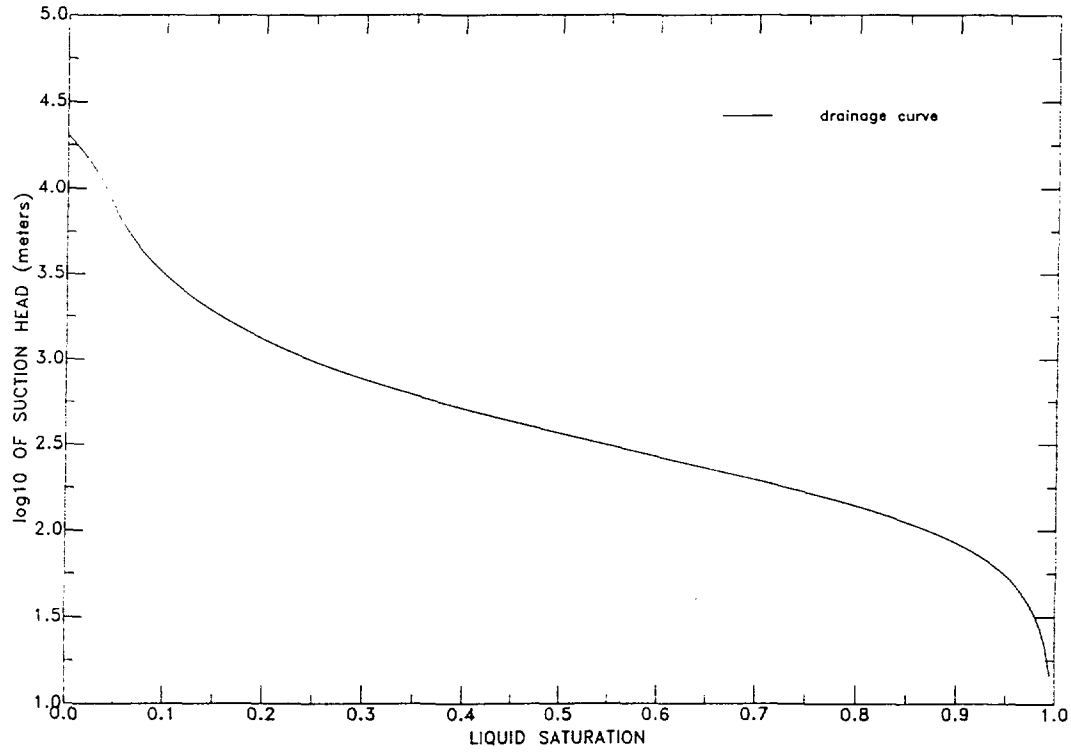

Figure 3. Log of the absolute value of suction head versus liquid saturation for sample G4-6 cored at a depth of 1158 feet within the repository horizon at Yucca Mountain.

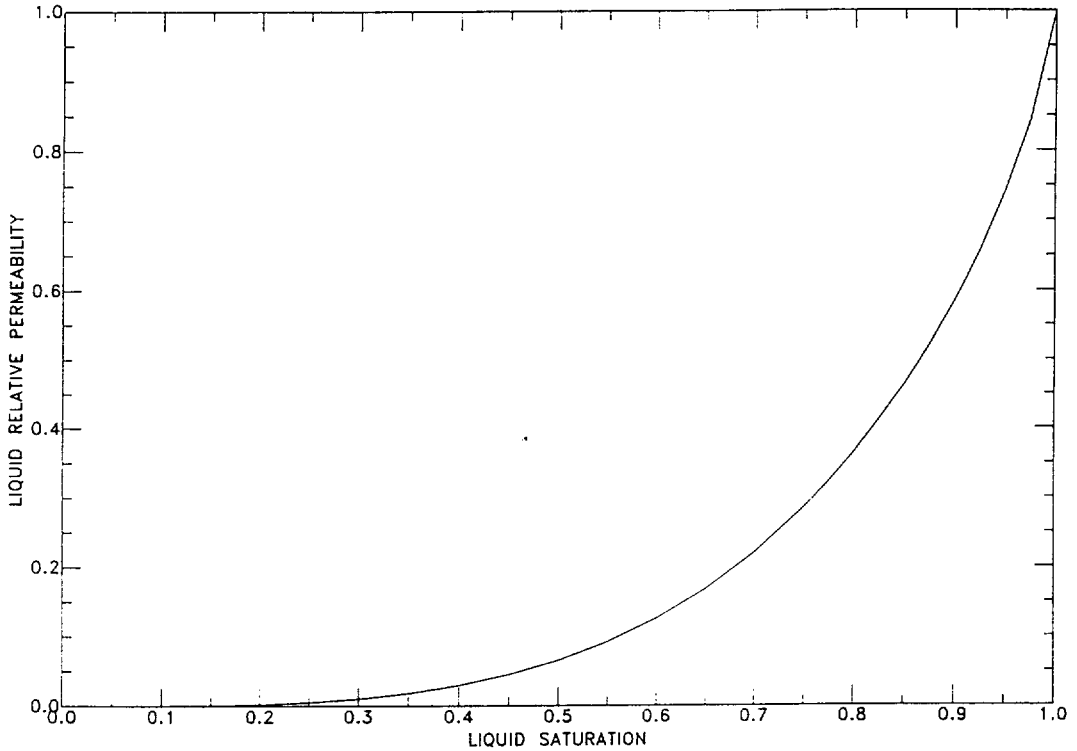

Figure 4. Liquid relative permeability versus liquid saturation for a 100 μm fracture.

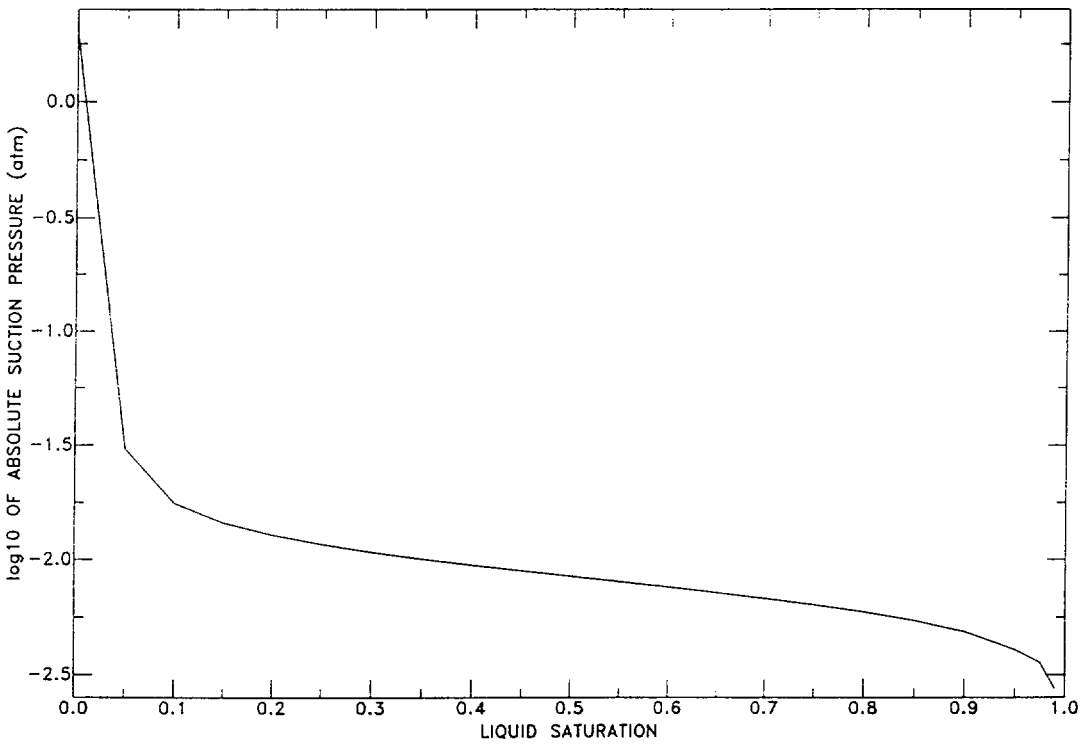

Figure 5. Log of the absolute value of suction pressure versus liquid saturation for a 100 μm fracture.

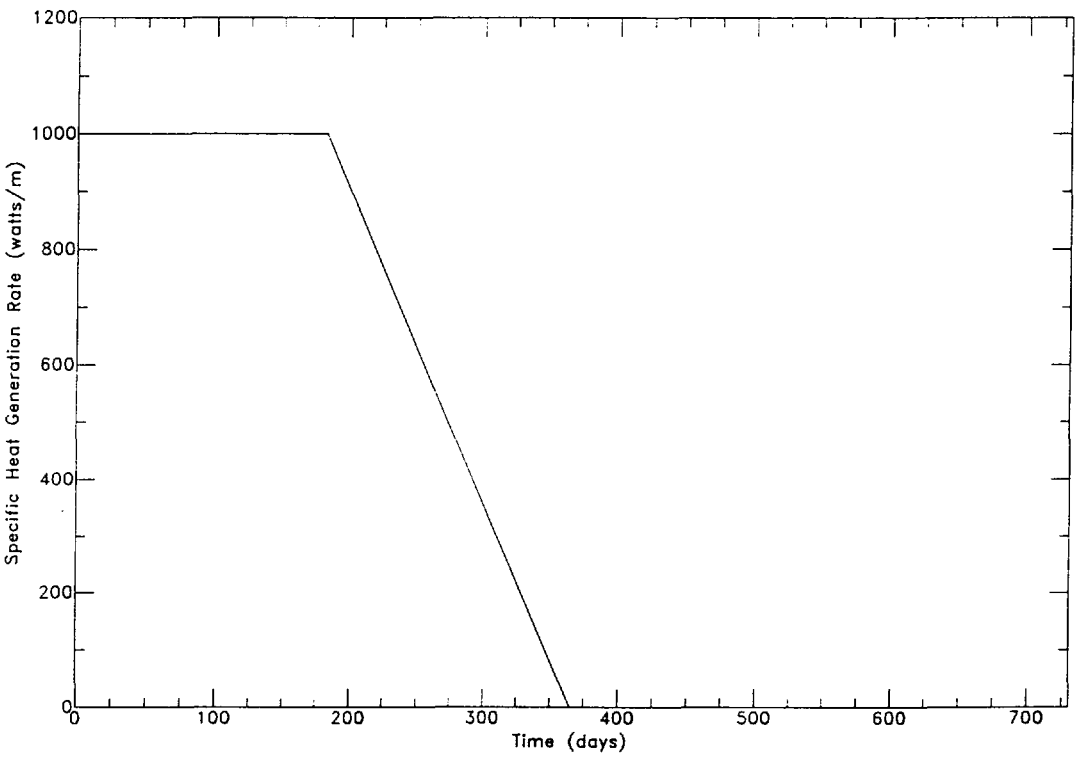

Figure 6. Specific heat generation rate for the EBDT heater.

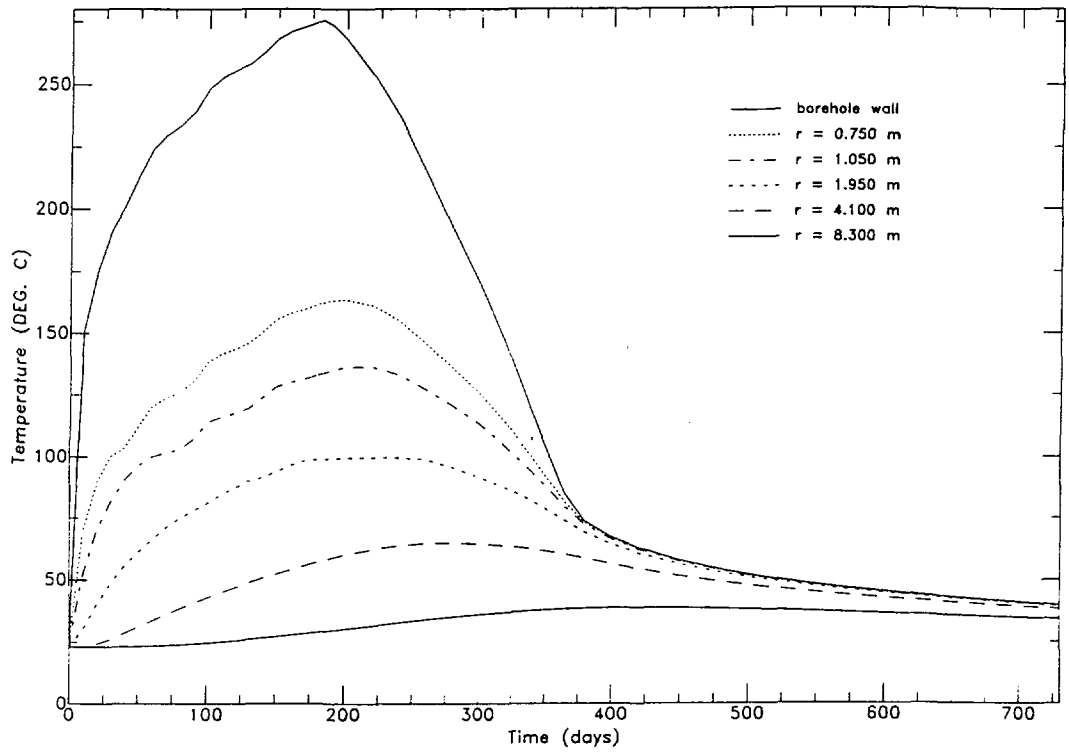

Figure 7. Temperature history for six different radial locations which lie along the midplane of the matrix block.

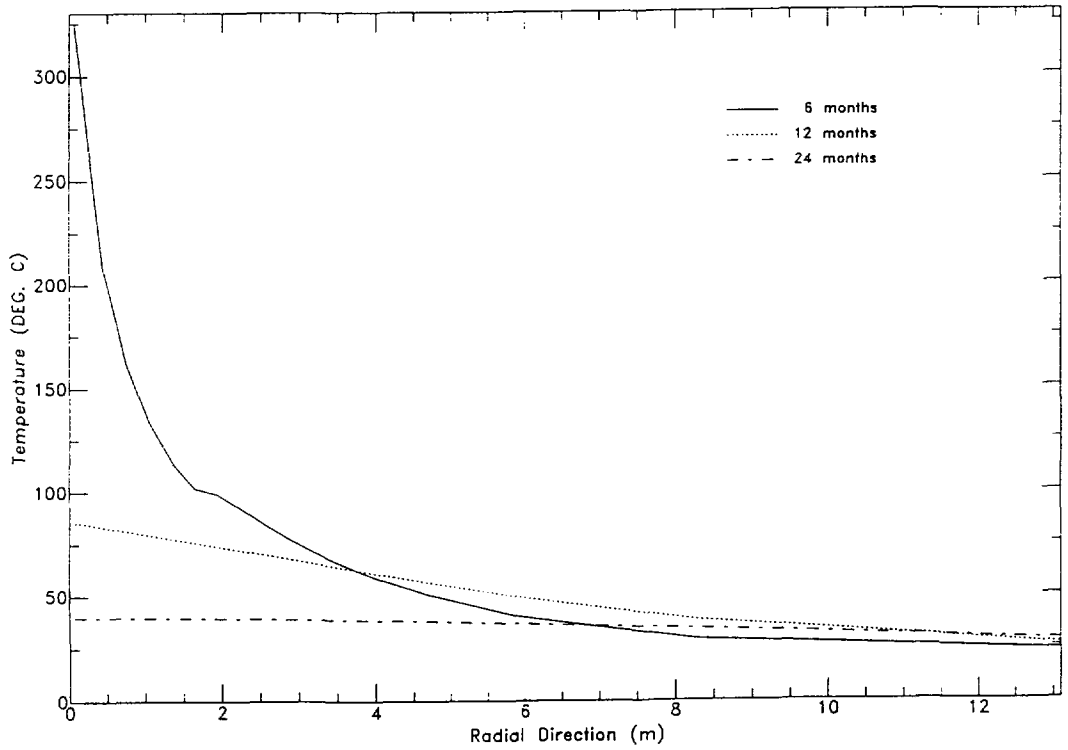

Figure 8. Temperature versus radial distance from the heater axis at the end of each of the three stages (t = 6, 12, and 24 months). Note that the temperature profiles are plotted along the midplane of the matrix block.

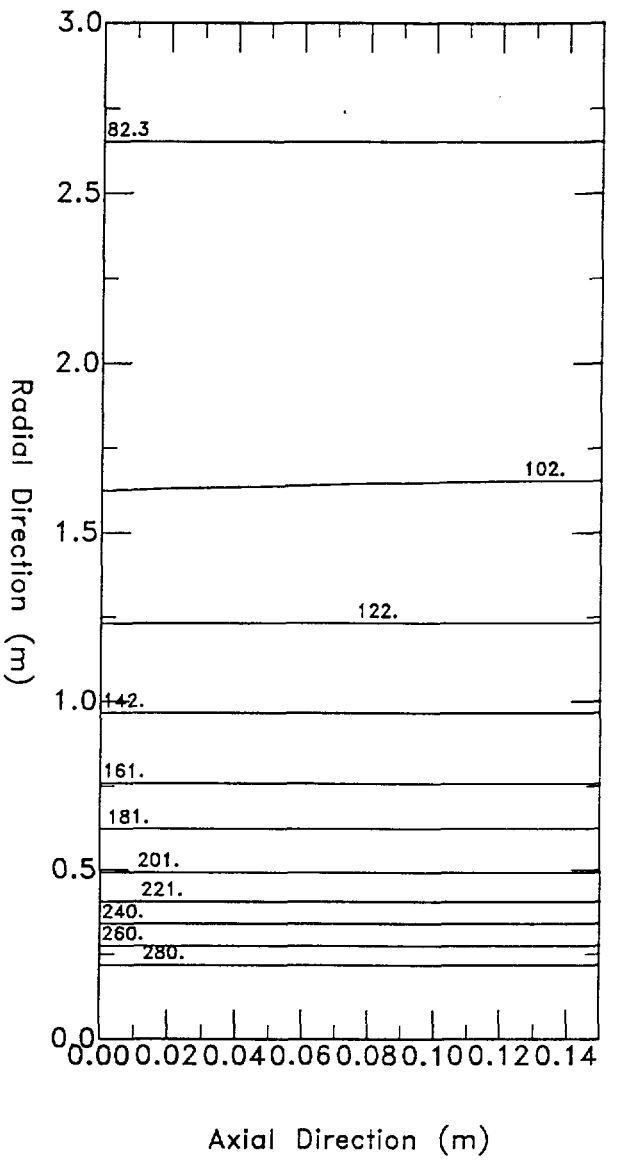

Figure 9. Contour plot of temperature within both the fracture and matrix at the end of the full-power heating stage (t = 6 months). Note that axial distances are exaggerated by a factor of 10.

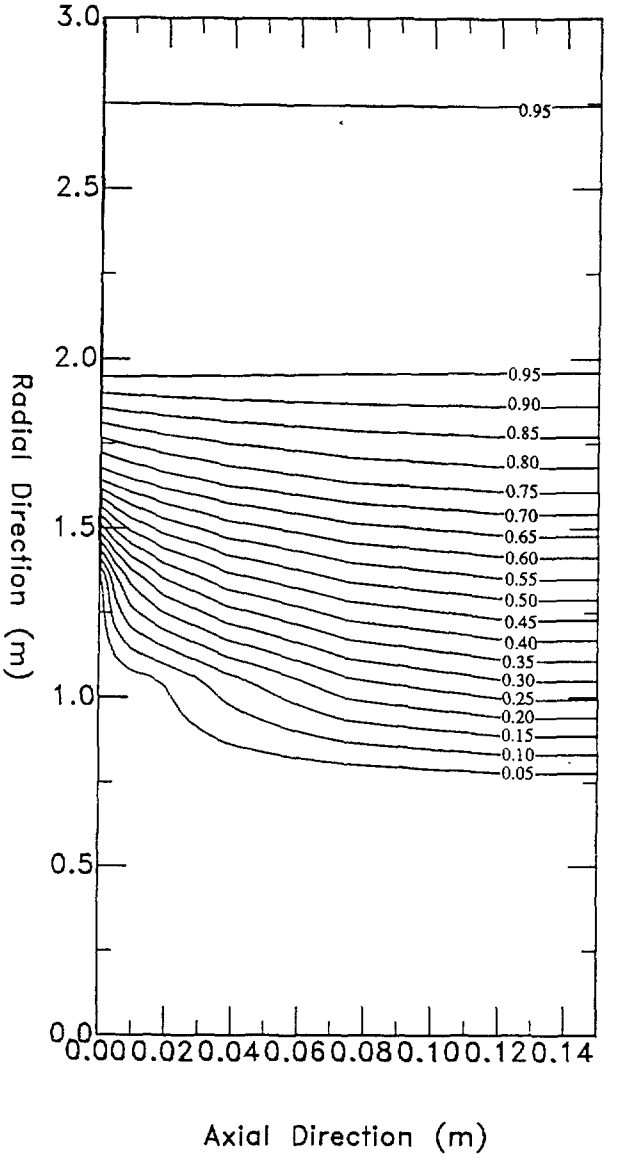

Figure 10. Contour plot of saturation within both the fracture and matrix at the end of the full-power heating stage (t = 6 months). Note that axial distances are exaggerated by a factor of 10.

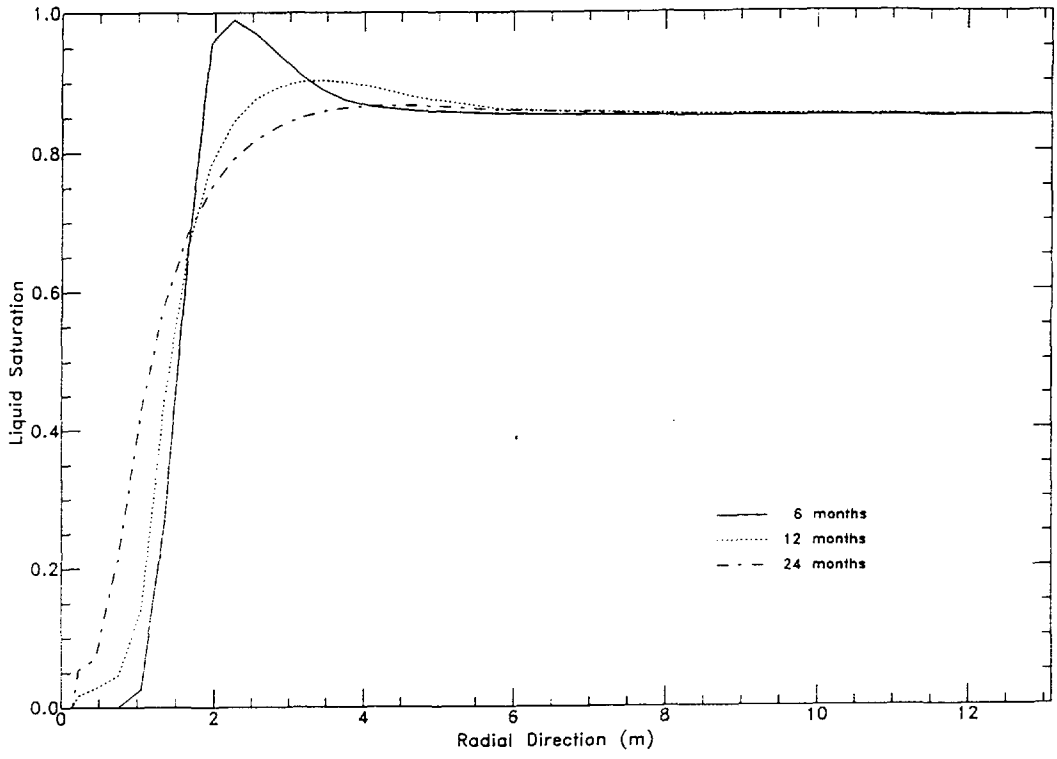

Figure 11. Liquid saturation versus radial distance from the heater axis at the end of each of the three stages (t = 6, 12, and 24 months). Note that saturation profiles are plotted in the matrix block at an axial distance of z = 1.0 *cm* from the fracture midplane.

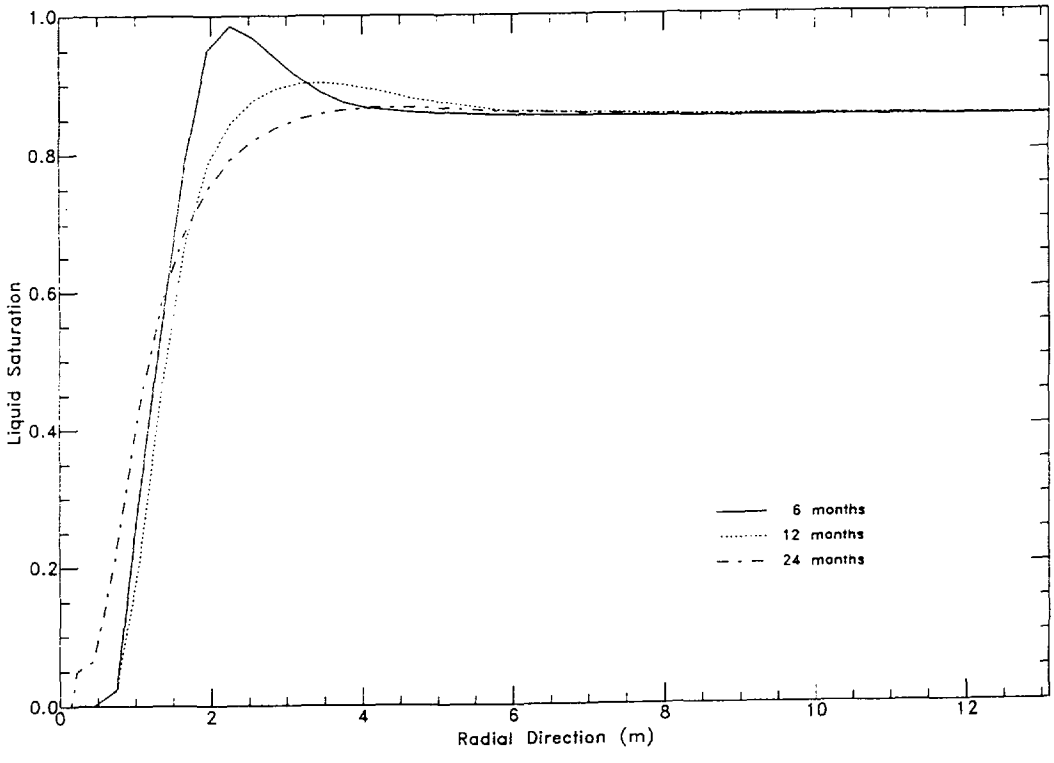

Figure 12. Liquid saturation versus radial distance from the heater axis at the end of each of the three stages (t = 6, 12, and 24 months). Note that saturation profiles are plotted along the midplane of the matrix block.

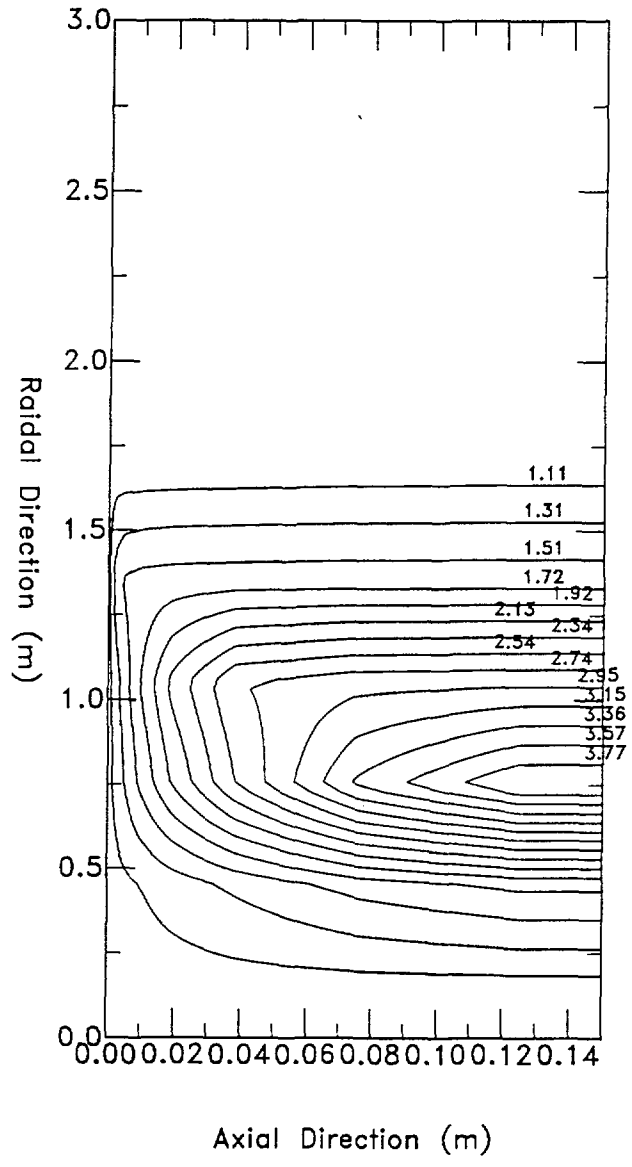

Figure 13. Contour plot of gas-phase pressure (*atm*) within the fracture and matrix at the end of the full-power heating stage (t = 6 months). Note that axial distances are exaggerated by a factor of 10.

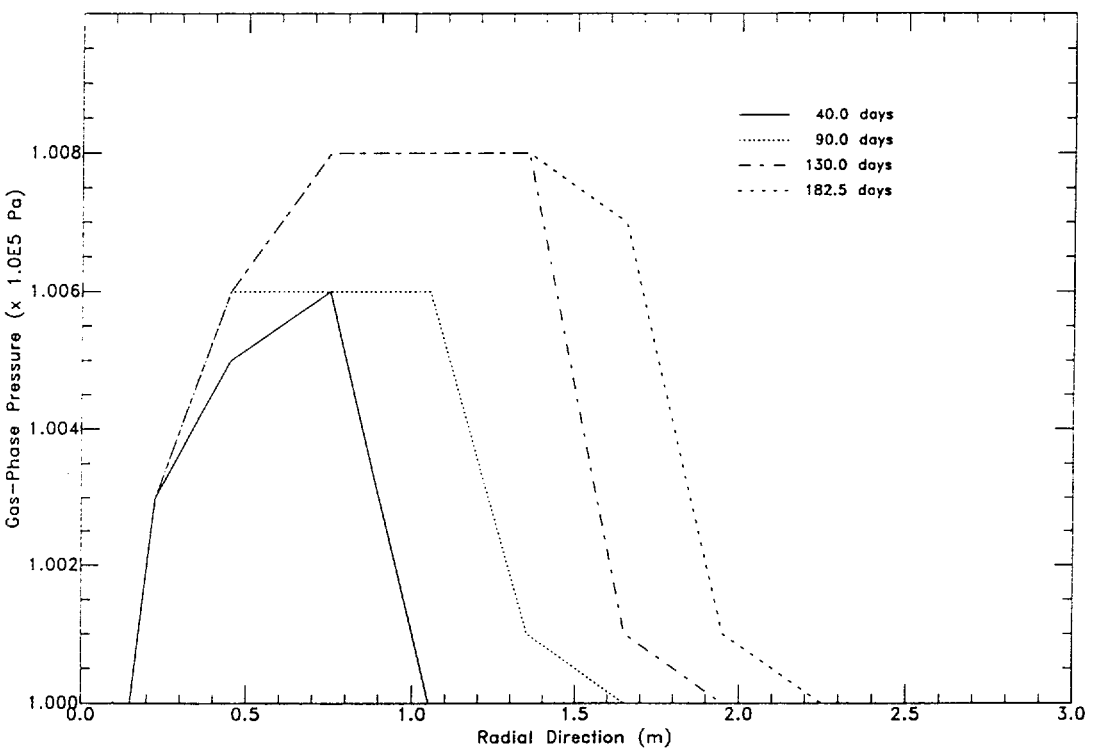

Figure 14. Gas-phase pressure profile along the midplane of the fracture at four different times during the full-power heating stage (t = 40.0, 90.0, 130.0, and 182.5 days).

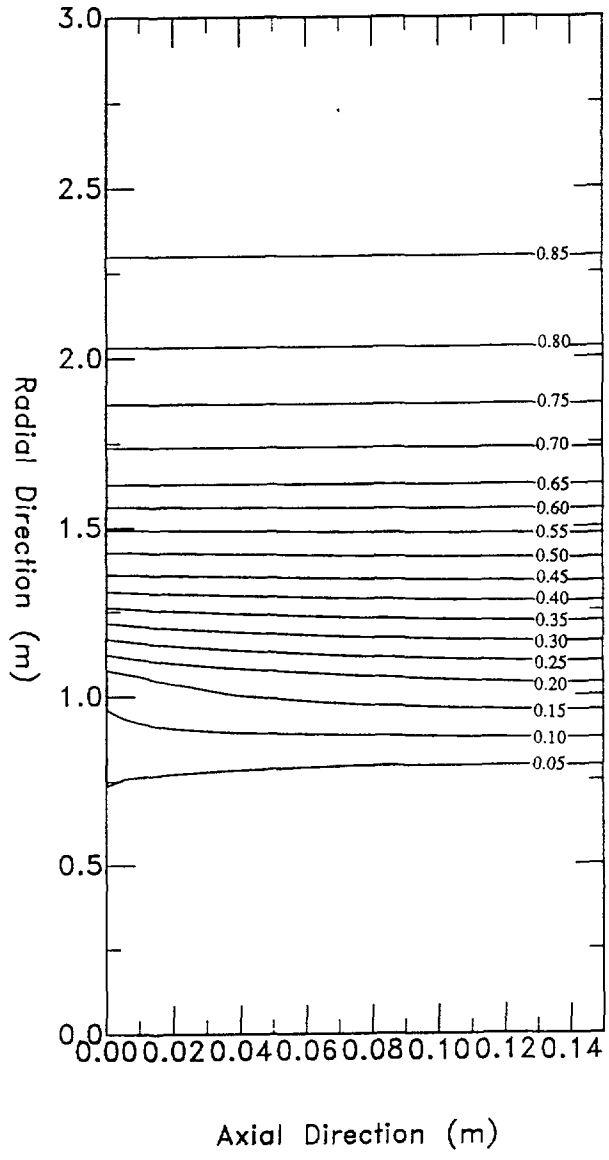

Figure 15. Contour plot of saturation within both the fracture and matrix at the end of the rampdown stage (t = 12 months). Note that axial distances are exaggerated by a factor of 10.

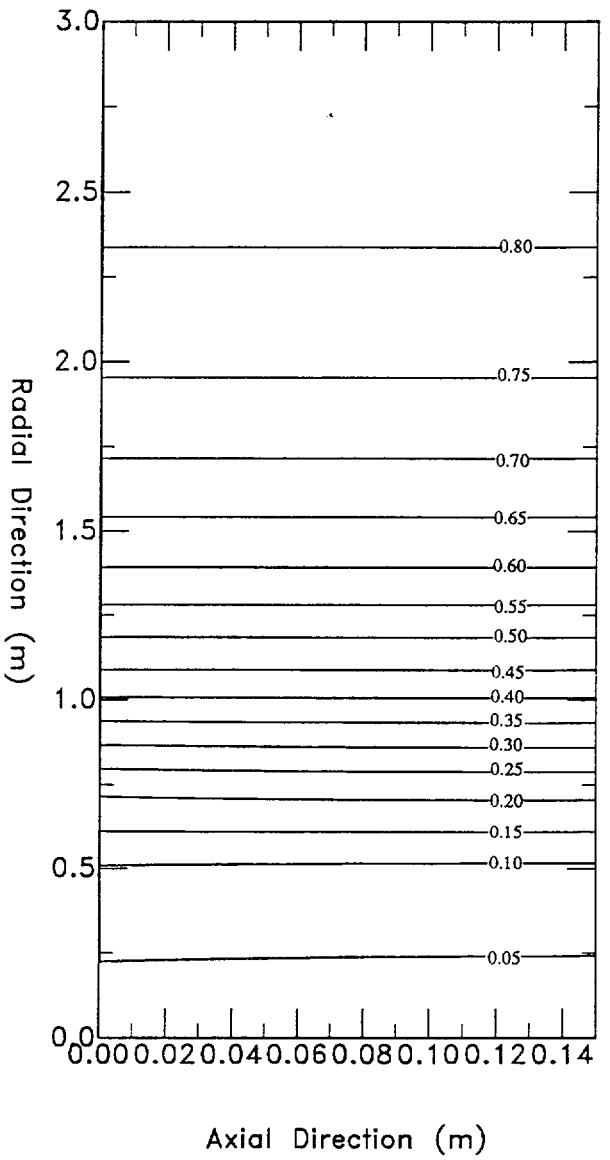

Figure 16. Contour plot of saturation within both the fracture and matrix at the end of the cooling stage (t = 24 months). Note that axial distances are exaggerated by a factor of 10.

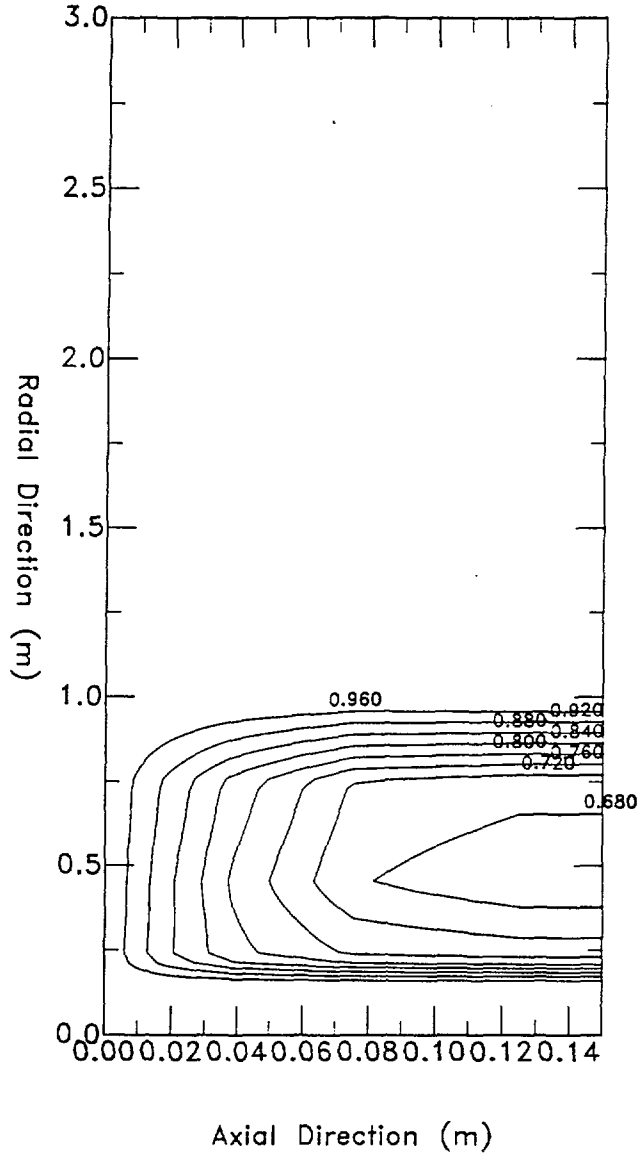

Figure 17. Contour plot of gas-phase pressure (*atm*) within the fracture and matrix at the end of the rampdown stage (t = 12 months). Note that axial distances are exaggerated by a factor of 10.